Noname manuscript No.

(will be inserted by the editor)

Setting up a Large-Eddy Simulation to Focus on the Atmospheric Surface Layer

Einara Zahn · Elie Bou-Zeid

Received: DD Month YEAR / Accepted: DD Month YEAR

6 Abstract

Large-eddy simulations (LES) above forests and cities typically constrain the simulation domain to the first 10-20\% of the Atmospheric Boundary Layer (ABL), aiming to represent the finer details of the roughness elements and sublayer. These simulations are also commonly driven by a constant pressure gradient term in the streamwise direction and zero stress at the top, resulting 11 in an unrealistic fast decay of the total stress profile. In this study, we investi-12 gate five LES setups, including pressure and/or top-shear driven flows with and without the Coriolis force, with the aim of identifying which option best repre-14 sents turbulence profiles in the atmospheric surface layer (ASL). We show that 15 flows driven solely by pressure not only result in a fast-decaying stress profile, 16 but also in lower velocity variances and higher velocity skewnesses. Top-shear driven flows, on the other hand, better replicate ASL statistics. Overall, we 18 recommend, and provide setup guidance for, simulation designs that include 19 both a large scale pressure forcing and a non-zero stress and scalar flux at the top of the domain, and that also represent the Coriolis force. Such setups 21 retain all the forces used in typical full ABL cases and result in the best match 22 of the profiles of various statistical moments. 23

Keywords Canopy flows \cdot Large-Eddy Simulation \cdot Surface Layer

26 1 Introduction

25

- 27 Propelled by an increase in computational resources and the continuous im-
- 28 provement in physics parameterization of atmospheric processes, Large-Eddy
- ²⁹ Simulations (LES) have been widely applied to investigate turbulence in the

Einara Zahn E209 Engineering Quadrangle E-mail: einaraz@princeton.com

52

53

54

55

57

58

59

61

62

63

65

66

67

68

71

72

73

Atmospheric Boundary Layer (ABL) in the past decades (Stoll et al. 2020). While its first applications aimed at reproducing the ABL structure above flat, homogeneous surfaces (Deardorff 1970; Mason 1989; Kosović and Curry 32 2000; Bou-Zeid et al. 2005; Churchfield et al. 2012; Huang et al. 2011; Ghan-33 nam and Bou-Zeid 2021), LES scope quickly expanded to represent more com-34 plex surface features such as surface heterogeneity (Avissar and Schmidt 1998; 35 Bertoldi et al. 2007; Esau 2007; van Heerwaarden et al. 2014; Allouche et al. 36 2023; Fogarty and Bou-Zeid 2023), vegetation (Shaw and Schumann 1992; Su 37 et al. 1998; Albertson et al. 2001a,b; Patton et al. 2001; Watanabe 2004; Shaw 38 and Patton 2003; Yue et al. 2007; Huang et al. 2013; Bailey and Stoll 2013; Pan et al. 2014), wind turbines (Calaf et al. 2010; Wu and Porté-Agel 2011; 40 Chatelain et al. 2013; Bastankhah and Porté-Agel 2014; Troldborg et al. 2014; 41 Hezaveh and Bou-Zeid 2018), and buildings (Xie and Castro 2009; Hellsten et al. 2015; Anderson et al. 2015; Li and Wang 2018; Llaguno-Munitxa and 43 Bou-Zeid 2018; Shin et al. 2021). Coupling of LES with models representing 44 other atmosphere processes, such as cloud microphysics and land-atmosphere 45 interactions (Heus et al. 2010a; Maronga et al. 2015), as well as coupling with mesoscale models (Talbot et al. 2012; Muñoz-Esparza et al. 2021), have also 47 led to more realistic simulations of ABL evolution. With this expansion of 48 applications came challenges related, among others, to the range of scales an 49 LES can resolve.

Turbulence in the atmosphere exhibits an extensive range of eddy sizes, spanning from a few millimeters up to the length of the very large scale motions (VLSMs) that can be multiple times the ABL height. The surface also features a range of scales, from the leaf to the wind turbine, that need to be captured or parameterized. Thus, the higher the resolution of the simulation, the finer the details of the modeled turbulent structures and surface that can be dynamically captured. For instance, Sullivan and Patton (2011) compared the convective ABL structure under increasingly more refined domains, varying from 32³ to 1024³ grid points, and showed continued improvement in the representation of higher-order statistics. Such high-resolution simulations, however, are not always feasible given the computational resources required, and not always desirable when the problem at hand requires a large number of simulations and setups. Thus, even if a 1024³ grid points simulation is attainable, the question of whether to expend the computing resources capturing the VLSMs or zooming in on the finer surface scale remains.

To circumvent these limitations and decrease the computational burden, many studies have implemented grid nesting (Sullivan et al. 1996; Khanna and Brasseur 1997; Talbot et al. 2012; Mirocha et al. 2013; Maronga et al. 2020) and/or grid stretching (Heus et al. 2010b; Hellsten et al. 2021; Sauer and Muñoz-Esparza 2020; Llaguno-Munitxa et al. 2017). The former method involves the use of two or more meshes, where the finer ones are nested inside the coarser grids. Grid stretching, on the other hand, consists of progressively increasing the grid space, keeping a refined grid close to the surface. Both approaches improve the representation of details in the ASL, and have been successfully employed, for instance, to study canopy flows (Patton et al. 2003;

Cassiani et al. 2008; Huang et al. 2009; Klosterhalfen et al. 2019). Nonetheless, despite their potential and the moderate increase in computational demand, these alternatives are still not widely adopted, possibly due to their relatively complex implementation requirements. Most LES studies thus continue to use either large domains that coarsely span the full ABL, or smaller ones that focus on the surface features and layer, with higher resolutions.

Of specific relevance to the present paper, studies interested in turbulence in the ASL or an even shallower layer — such as the canopy and roughness sublayers of forests or cities — opt for decreasing the simulated domain depth so as to better represent these roughness features near the surface. Thus, domain heights above vegetation and cities are typically between 3 and 10h, where his the mean canopy height (Shaw and Schumann 1992; Watanabe 2004; Shaw and Patton 2003; Yue et al. 2007; Mao et al. 2008; Pan et al. 2014; Li et al. 2016b; Grylls and van Reeuwijk 2021; Joshi and Anderson 2022), representing only a fraction of the ABL extent. Such configurations are particularly beneficial for research scenarios that require suites of simulations, where decreasing the computational burden allows better spanning of the problem's parameter space. It would also be a remiss not to underline here that, in addition to faster and simpler simulations, such setups reduce the rapidly increasing energy demand of geophysical simulations: NCAR's Wyoming Supercomputing Center, designed as one of the most energy efficient data centers in the world, still uses about 4-8 MW of power (depending on weather and computing loads), that are equivalent to the needs of about 2000-4000 US homes (Potomac-Hudson Environmental Team 2010).

In terms of LES design, full ABL simulations typically include an externally-imposed synoptic pressure gradient, often expressed as an equivalent geostrophic velocity, as well as the Coriolis force. At the top of the domain, zero stress and zero scalar flux conditions are imposed, even when an inversion overlaid by damping layer are added below the upper boundary. In all cases, a wall model is also needed to compute the surface stress and flux. The final flux profiles are then characterized by a slow decay of fluxes of momentum and scalars from a maximum at the surface to zero at the top of the domain (with more activity near the top of the ABL when an inversion is included). In such setups, a flux decrease of around 10% is observed across the Atmospheric Surface Layer (ASL) (~100 m), which is in agreement with predictions and observations.

Simulations with reduced domain heights above canopies are usually setup in a very similar way to full ABL simulations, with an imposed external pressure forcing, assuming a stress free and zero scalar flux top boundary condition. As a result, a fast decaying stress profile balancing the pressure term is seen under steady conditions, deviating from the expected constant flux (or approximately constant stress) layer. The imposed condition of zero scalar flux at the top also results in rapid and continuous increase of the scalar concentrations in the domain, and a flux profile decreasing to zero very close to the canopy top. These characteristics are not representative of the atmospheric surface layer as shown in various field experiments or deduced from full-ABL simulations. However, while a few studies compared simulations above canopies

124

125

127

128

129

131

132

133

135

138

139

142

143

145

146

147

149

150

151

152

153

154

155

157

driven by pressure or shear (Su et al. 1998; Watanabe 2004; Su and Paw U 2023; Sanemitsu et al. 2023), the question of how to improve the representation of the ASL in small domains remains largely unexplored. To bridge this gap, this study investigates the impact of different flow forcings and top boundary conditions on small-domain simulations representing the ASL. Five different simulations using a combination of imposed pressure, shear and/or Coriolis are compared against the results obtained from a full ABL simulation to determine which one provides the most realistic ASL flow structures.

2 Simulations 130

The LES code used here has been extensively evaluated in previous studies (Bou-Zeid et al. 2005; Kumar et al. 2006; Huang and Bou-Zeid 2013; Li and Bou-Zeid 2019). It solves the spatially filtered incompressible continuity (1) and Navier-Stokes (2) equations under the Boussinesq approximation, as well as a budget equation for a scalar q

$$\frac{\partial \widetilde{u}_i}{\partial r_i} = 0,\tag{1}$$

$$\frac{\partial \widetilde{u}_i}{\partial x_i} = 0,$$

$$\frac{\partial \widetilde{u}_i}{\partial t} + \widetilde{u}_j \left(\frac{\partial \widetilde{u}_i}{\partial x_j} - \frac{\partial \widetilde{u}_j}{\partial x_i} \right) = -\frac{\partial p^*}{\partial x_i} - \frac{\partial \tau_{ij}}{\partial x_j} + f_c \epsilon_{ij3} (\widetilde{u}_j - u_j^G) + P_i,$$
(2)

$$\frac{\partial \widetilde{q}}{\partial t} + \widetilde{u}_j \frac{\partial \widetilde{q}}{\partial x_j} = -\frac{\partial \pi_j}{\partial x_j},\tag{3}$$

where \widetilde{u}_i are the resolved (filtered) velocity components (i=1,2,3) and \widetilde{q} is the resolved passive scalar. p^* is a modified resolved dynamic pressure that also includes the resolved and subgrid-scale (SGS) turbulent kinetic energy (Bou-Zeid et al. 2005); τ_{ij} is the anisotropic part of the SGS stress tensor; $f_c = 1.4 \times 10^{-4} \text{ s}^{-1}$ is the Coriolis parameter; π_j is the SGS scalar flux; and ϵ_{ijk} is the Levi-Civita symbol. Finally, the flow can be driven by a large scale pressure imposed either in terms of a geostrophic velocity $u_i^G = (u^G, v^G, 0)$, or as a constant body force term P_i . All our simulations are neutral, and thus the buoyancy term was neglected in the momentum equation.

The numerical details of the code are typical of other Large-Eddy Simulations, including a pseudo spectral scheme in the horizontal and a second-order finite difference in the vertical. Second order Adams-Bashforth is used for time stepping. Additional details on the numerics as well as the SGS and wall models can be found elsewhere (Bou-Zeid et al. 2005; Li et al. 2016a).

To investigate the effects of top boundary conditions as well as imposed driving forces on the flow, we designed six simulations as represented in Table 1. Different configurations include one or more of the following driving forces and/or boundary conditions: pressure gradient imposed as a constant $-d\overline{p}/dx$ $(P_1 \text{ in the equation above, the overbar represents the Reynolds average), de$ noted by P_x in the case name, or in terms of geostrophic velocity, where the cases are denoted as \mathbf{U}^G . In addition, these simulations might also contain the Coriolis term (C), stress (S) and/or scalar flux (F) at the top of the domain.

Simulations driven by shear (S), meaning that they incorporated a top stress, were accomplished by imposing the subgrid-scale component at the upper boundary of the domain L_z as follows:

$$\tau_{xz}(L_z) = \cos \alpha_\tau u_S^2,
\tau_{yz}(L_z) = \sin \alpha_\tau u_S^2,$$
(4)

where u_S^2 is the kinematic stress magnitude to be imposed at the domain top; (τ_{xz}, τ_{yz}) are its components in the streamwise and cross-stream directions, respectively; and α_{τ} is the angle between the stress vector and the x-axis. Similarly, a constant scalar flux is imposed at the top as

$$\pi_z(L_z) = F_{\text{top}} = -F_{\text{bottom}},$$
(5)

where the top flux (F_{top}) has the opposite sign of the flux imposed at the surface (F_{bottom}) , ensuring no accumulation of scalar in the domain that would allow scalar statistics to reach a steady-state. Thus, while all simulations impose a constant surface flux F_{bottom} , only simulations differentiated by "F" in Table 1 additionally include $F_{\text{top}} = -F_{\text{bottom}}$ (i.e., the remaining cases maintain the usually adopted configuration $F_{\text{top}} = 0$). Moreover, note that F_{top} can be adjusted in such a way that a 10–20% flux decay from the surface to the top of the domain can be simulated.

The first case (Full ABL) represents a typical neutral ABL simulation that extends to $L_z=1$ km above the surface, and is driven by a large scale forcing, here imposed as $u^G=8$ m/s and $v^G=0$ m/s, with zero stress and flux top boundary conditions. This setup results in a geostrophic wind above the ABL aligned in the x direction. The following five simulations assume a shorter domain representing the bottom 14% of the full ABL simulation (i.e., 140 m), which is typically the range adopted when representing forests or urban canopies, where $3-10h\approx 60-200$ m for h=20 m, but the implications should be similar for the deeper domains used for wind energy applications or taller buildings.

Case 2 (S+U^G+C+F) was designed to represent the same balance of forces found at z=140 m in the full ABL case. To this end, we first computed the stress terms at z=140 m in case 1, finding $\tau_{xz}/u_{S,140\,\mathrm{m}}^2=-0.9947$ and $\tau_{yz}/u_{S,140\,\mathrm{m}}^2=0.1029$ ($\alpha_{\tau}=174.1^{\circ}$ in equation (4)), where τ_{iz} is the total horizontal stress (resolved + SGS) at 140 m and $u_{S,140\,\mathrm{m}}=(\tau_{xz}^2+\tau_{yz}^2)^{1/4}=0.30$ m/s. This stress term was then imposed as the SGS contribution at the top boundary. In addition to retaining the Coriolis term, case 2 was also driven by the same large scale pressure force imposed in the full ABL case ($u^G=8$ m/s, $v^G=0$ m/s). Our profiles for the full ABL results (case 1) are available in the Supplementary Information and can be used as a starting point to design shallow domain simulations in other studies of the neutral barotropic ABL. However, new full-ABL simulations would be required to take stability or baroclinicity into account.

The roughness length, $z_0 = 0.05$ m, was kept constant in all cases. The same number of grid points was used in all small domain simulations ($N_x = N_y = 144$,

Table 1 Summary of simulations compared in this study. Different combinations include a top stress term (S), pressure gradient imposed in terms of geostrophic wind \mathbf{U}^G or a constant streamwise gradient (\mathbf{P}_x), and Coriolis (C). In addition, they might also include a constant scalar flux at the top (F) matching the flux at the bottom. Case 1 simulates the entire ABL, while the remaining five cases simulate a reduced domain of 140 m. A constant stress $(\tau_{xz}/u_S^2, \tau_{yz}/u_S^2) = (-0.9947, 0.1029)$, as well as a constant scalar flux ($F_{\rm top} = -F_{\rm bottom}$, where $F_{\rm bottom}$ is the flux imposed at the surface), were used as top boundary condition in cases 2, 3, 4 and 5. A large scale pressure forcing with $u^G = 8$ m/s and $v^G = 0$ m/s was included in cases 1, 2, and 4, while a normalized pressure gradient (L_z/u_*^2) $dP/dx_1 = 1$ drives the flow in 6. Output normalization removes any distinction between the simulations imposing a geostrophic wind equivalent to the pressure gradient or a normalized value.

	ID	Forcing	# grid points	Domain
1	Full ABL	Pressure + Coriolis	(288, 288, 216)	(6, 6, 1) km
2	$\mathrm{S}{+}\mathrm{U}^G{+}\mathrm{C}{+}\mathrm{F}$	Stress + Pressure + Coriolis + Flux	(144, 144, 108)	(0.84, 0.84, 0.14) km
3	S+C+F	Stress + Coriolis + Flux	(144, 144, 108)	(0.84, 0.84, 0.14) km
4	U^G+C+F	Pressure + Coriolis + Flux	(144, 144, 108)	(0.84, 0.84, 0.14) km
5	S+F	Stress + Flux	(144, 144, 108)	(0.84, 0.84, 0.14) km
6	P_x	Pressure	(144, 144, 108)	(0.84, 0.84, 0.14) km

and N_z =108), while results for the full ABL case use double the number of grid points. While this results in a coarser resolution in the full domain, we note that the full ABL results were not significantly modified when a coarser grid (same number of nodes as in cases 2–6) was used, indicating good grid convergence for this case (comparison for first, second and third-order statistics for the full ABL case for both resolutions are included in Appendix A, Figures 4 and 5). It is thus worth emphasising that the precursor ABL simulation used to design the shallow domain can be run at a much lower resolution than case 1 used here. Only the stress vector (resolved+SGS), and potentially the scalr flux, at a height z corresponding to the top of the shallow domain is needed from the large domain simulation, and this variable is almost insensitive to domain resolution as our grid sensitivity tests suggest (also, for instance, see Fig. 9 in Berg et al. (2020)).

Similarly, results obtained for case 2 using double the resolution did not alter the conclusions of this paper (comparison not shown here), and thus only results obtained using the lower resolution grid is shown for small domain simulations. All results presented here were obtained from spatial and temporal averages (over at least 20 eddy turnover times, L_z/u_*) after a warm up period during which steady-state conditions were achieved. u_* and $q_* = \pi_{\rm bottom}/u_*$ were computed at the surface from the SGS contribution, while quadrant analyses, variances, turbulent kinetic energy, and skewness were computed based on the resolved part.

20 3 Results and discussion

3.1 Mean profiles

The normalized streamwise (\overline{u}/u_*) and cross-stream (\overline{v}/u_*) velocity profiles are shown in Figure 1a–b. Similar to results reported by Su et al. (1998) and Watanabe (2004), the mean profiles obtained for cases with an imposed top stress are characterized by a sharp gradient at the top of the domain (above z>110 m; dashed line in the figures), which is a consequence of inefficient turbulence mixing by the smaller eddies present near the top boundary, requiring larger gradients to drive the constant fluxes. Nonetheless, results below this region are unaffected and follow the expected ABL statistics. Thus, as suggested in previous studies (Su et al. 1998; Watanabe 2004), we recommend ignoring the solution in the top $\approx 20\%$ of the domain when a stress boundary condition (and/or a constant scalar flux) is used, which should be taken into account when designing the height of the domain. Alternatively, setups that impose the top stress and scalar flux across a finite-depth sponge region near the top could be tested in the future to reduce the steep gradients.

As expected, the simulations with an imposed top stress vector resulted in a non-zero \overline{v} profile, although the wind angle also depends on whether a pressure term or Coriolis were present. The best agreement with the full ABL case is the simulation including a top stress, pressure, and Coriolis (S+U^G+C+F). The simulations with the cross-stream velocity profiles that deviate most from full ABL reference case are S+C+F and U^G+C+F, which include Coriolis, and either S or U^G. This is understandable as these are the ones that produce an unrealistic force balance by including only 2 of the 3 forces acting in an Ekman boundary layer. Nonetheless, good agreement is seen for all mean wind profiles, $\overline{M} = (\overline{u}^2 + \overline{v}^2)^{1/2}$, in Figure 1c. Thus, while the wind angle varies, the mean wind profile normalized by the surface friction velocity, up to 100 m, is less sensitive to the choice of forcings and top boundary condition.

The profiles of the mean scalar quantity, represented as $(\overline{q}-Q)/q_*$, where Q is the domain volume average of the scalar, are shown in Figure 1d. Note that this subtraction is necessary given that the concentrations increase over time in the absence of scalar sinks (including in the full ABL simulation), and particularly in case P_x where the flux is concentrated in an even shallower domain. Despite the scalar accumulation, we verified that $(\overline{q}-Q)/q_*$ is stationary. Overall, the worst agreement with the full ABL profiles is observed for case U^G+C+F , which overestimates concentrations below 50 m. Simulation P_x , on the other hand, best replicates the full ABL profile, although all simulations with a top stress also follow the reference closely.

3.2 High-order turbulent statistics

Typical LES setups above forests and cities include an external pressure gradient in the streamwise direction as the main driver of the flow. Under these

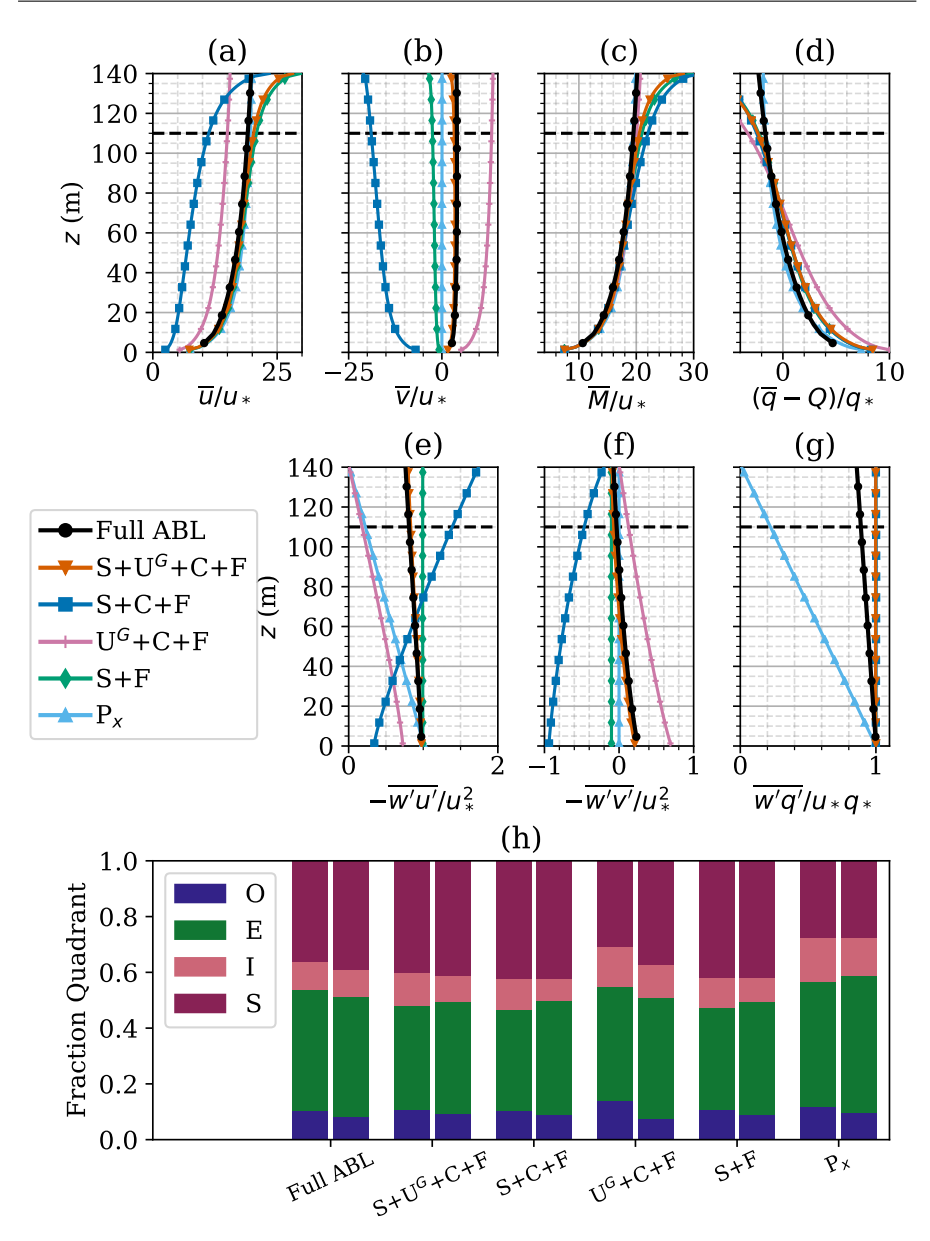


Fig. 1 Mean profiles of streamwise velocity, \overline{u} a), cross-stream, \overline{v} b), mean wind speed $\overline{M}=(\overline{u}^2+\overline{v}^2)^{1/2}$, and scalar concentration d), where u_* is the friction velocity, Q is the volume averaged scalar concentration, and q_* is the turbulent scale of the scalar q. Profile of streamwise e) and cross-stream momentum f), and scalar flux g). Fluxes in plots e–g include the SGS component. Dashed black line represents the height above which a sharp gradient is observed when a top stress drives the flow. Plot h) shows the contributions from sweeps (S), ejections (E), inward (I) and outward (O) interactions to fluxes of momentum (left bars) and scalar (right bars) at z=100 m.

conditions, a balance between the flux divergence term and the pressure forcing, under steady state conditions, results in a linear decrease in momentum flux from a maximum value near the surface to zero at the top of the domain (case P_x in Figure 1e–f). While routinely shown across papers, this stress profile produced by shallow domains is not realistic in the surface layer, where a near constant profile is expected. Furthermore, inclusion of the Coriolis force invariably causes a more rapid (than linear) reduction in the stress, as shown in Ghannam and Bou-Zeid (2021) at various Rossby numbers. For instance, the simulation representing the full ABL shows a decrease of less than 20% up to 100 m of the domain, which is faster than linear (due the the finite Rossby number), but still slower than what would be produced by commonly-used shallow domains setups. The correct drop in the stress with height is closely replicated only by simulation $S+U^G+C+F$ (note that the results of that case and the full ABL overlap in Figures 1e and 1f).

As expected, a constant stress profile is obtained for case S+F since no other sinks or sources of momentum are present. However, the inclusion of a Coriolis term (case S+C+F) results in an unrealistic stress profile that increases with height. Since the forcing is applied at the top as a momentum source and the Earth surface acts as a momentum sink, the stress must decrease across the ABL as the Coriolis force acts to partially counter the resulting stress gradient force, reducing the total stress below its constant profile obtained without Coriolis (S+F case). Because u_* , by definition, is computed at the surface, the quantity $-\overline{w'w'}/u_*^2$ in Fig. 1e becomes larger than unity above $z\approx 70$ m for case S+C+F. For a fixed Coriolis parameter, the rate of stress decrease from top to bottom is also dependent on the Rossby number which will be affected by the magnitude of the imposed top stress and the Coriolis parameter (results not shown here). Overall, this unrealistic profile is not a surprise considering the nonphysical force balance used in this simulation.

Similarly, the scalar flux profile (Figure 1g) decays much faster in case P_x than the simulation for the full ABL predicts, the latter showing a flux decrease of $\approx 10\%$ at 100 m, as expected. Here, the use of a constant flux at the top of the domain ensures a constant flux layer that better matches conceptual models of the ASL, but one could also elect to impose a top flux that is reduced relative to the surface flux (as we do for stress), for example, to reproduce exactly the full domain profiles or account for fluxes at the inversion.

The contributions from different quadrants to the momentum and scalar fluxes are shown in Figure 1h, where the respective contributions from sweeps, ejections, and inward/outward interactions at z=100 m were quantified. For x-momentum flux, the different quadrants are defined as follows: sweeps (w'>0) and u'<0; ejections (w'>0) and u'<0; inward interactions (w'>0) and u'>0. For scalar flux, the following definition is adopted: sweeps (w'<0) and (u'<0); ejections (u'>0) and (u'<0); inward interactions (u'<0) and (u'<0); and outward interactions (u'<0) and (u'<0); and outward interactions (u'<0). The quadrants' contributions observed across all simulations are similar for momentum and scalar fluxes, but vary across simulations. Cases 1, 2, 3, and 5 show similar contributions from

309

310

311

312

313

314

315

316

317

319

320

321

322

323

324

325

326

327

328

329

330

331

332

333

334

335

336

337

338

339

341

342

343

345

346

348

349

350

352

sweeps and ejections ($\approx 40\%$ each), as well as for inward/outward interactions ($\approx 10\%$ each). Case 6 (P_x), on the other hand, results in almost double the contribution from inward interactions at the expense of a reduced contribution from sweeps. Overall, simulations including a top stress term are closer to the quadrant analyses observed for the ABL simulation.

Figure 2a-d) compares second and third-order moment profiles. Simulations driven only by pressure depart from the full ABL case more often than simulations that included a top stress term. As shown in Figure 2a-b, the normalized variances σ_u/u_* and σ_v/u_* decrease fast with height for cases U^G+C+F and P_x ; on the other hand, the normalized horizontal standard deviations for $S+U^G+C+F$ and S+F show a better agreement with the full ABL case. However, more differences are observed for the vertical standard deviation, σ_w/u_* , where flows driven solely by pressure underestimate the full ABL by up to 25%, while flows including a top stress overestimate the quantity by 20%. Here, direct comparison to the full ABL should be made with caution since the latter, with its coarser resolution, under-resolves the vertical velocity component more severely than the horizontal components, and we do not include the SGS components in the present comparison. As such, a higher (than the full ABL) vertical variance in a shallow domain certainly makes more sense than a lower one. In addition, it is expected that a shallow domain will directly interfere with fluctuations of vertical velocity, so a perfect match is not expected, but the differences between the shallow domains is significant and informative. The full ABL simulation used in this comparison does not have the same spatial resolution as the shallow domain cases. While the full ABL is simulated with dx = dy = 20.8 m and dz = 4.6 m, the remaining domains impose dx = dy = 5.8 m and dz = 1.3 m. Therefore, a more detailed quantitative comparison where the full ABL is simulated with the same spatial grid resolution is required to pinpoint the differences in higher-order statistics, but this is left for future studies gives its computing cost. In this case, a matching resolution full ABL would require $N_x \times N_y \times N_z = 1024 \times 1024 \times 756$ for a regular grid.

The profile of scalar standard deviation is shown in Figure 3d. Overall, more variability across the simulations is observed below 50 m, with simulation U^G+C+F showing the greatest departure from the full ABL profile. Case $S+U^G+C+F$, on the other hand, slightly overestimates the full ABL simulation near the surface, but it generally shows a nearly constant profile that follows the full ABL case. One here should note that the differences in mean scalar profiles noted before will result in differences in the gradient production term in the scalar variance budget, which then should result in differences in the variance profiles as observed here.

The skewnesses of u, v, and w are shown in Figure 2e–g. With exception of case U^G+C+F , all simulations converge to $sk_v \approx 0$ away from the surface. However, flows driven solely by a pressure term overestimate the magnitudes of sk_u and sk_w compared to the full ABL case, indicating higher asymmetry in the velocity distributions away from the surface. These results are in agreement with Watanabe (2004)'s findings, who compared shear and pressure

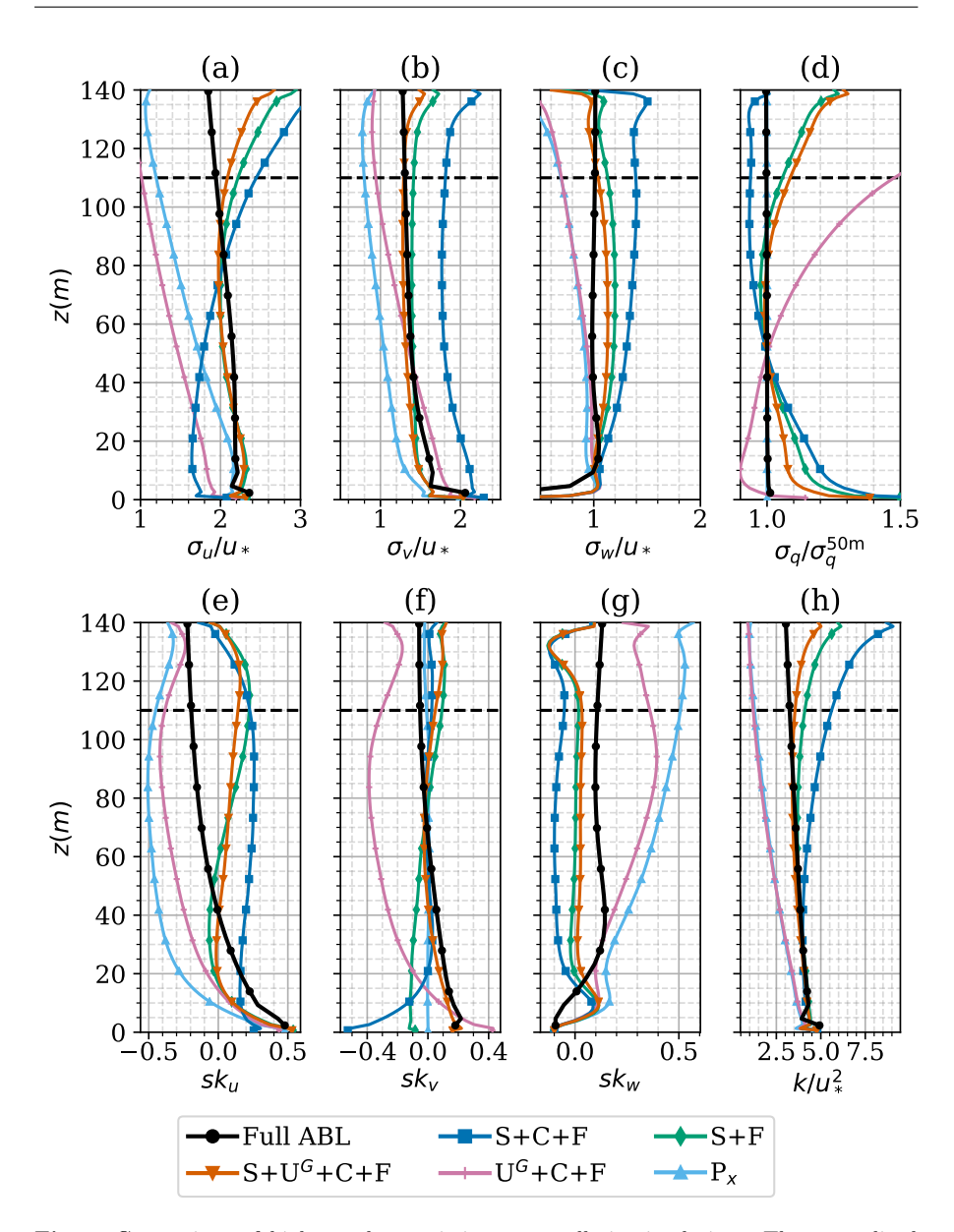


Fig. 2 Comparison of higher order statistics across all six simulations. The normalized standard deviations of velocity components and scalar are shown in plots a–d. Note that the scalar standard deviation, σ_q , was normalized by the standard deviation at z=50 m. The skewnessess of the three velocity components, as well as the turbulent kinetic energy (k) are shown in plots e–h. Standard-deviations, skewness and k only include resolved turbulence. Dashed black line represents the height above which a sharp gradient is observed when a top stress drives the flow.

driven flows above a canopy. The author found that the magnitudes of sk_u and sk_w in the streamwise pressure driven case increased with height, which is in disagreement with observations indicating that the skewness should decrease away from the surface. For the shear-driven flow, the author observed that u and w became more symmetric (i.e., skewnesses closer to zero) at around twice the canopy height, in agreement with a family portrait of observations across forests presented by Raupach et al. (1996). We also observed the same behavior in our simulations with a canopy model (more details in Appendix B). Thus, while none of the shear-driven flows perfectly captures the results from the full ABL case in terms of skewness, they result in more realistic profiles than flows driven solely by a pressure term.

Figure 2h suggests that shear-driven flows also better represent the turbulent kinetic energy (k) profile in the atmospheric surface layer. However, note that only the resolved part of k is included in the plot. The pressure driven flows, on the other hand, show a rapid decrease in k from the surface to the top of the domain. This is expected given the decrease in shear stress with height, which decreases the mechanical shear turbulent production far from the surface. Overall, in terms of k profile, simulations $S+U^G+C+F$ and S+F are superior in matching the full domain.

3.3 Instantaneous cross-sections

Figure 3 compares instantaneous horizontal slices of the streamwise velocity perturbation, u'/u_* , sampled at approximately 100 m. Simulations $S+U^G+C+F$ and S+F indicate the presence of similar structures with similar length scales, which was corroborated by analyses of the structure and autocorrelation functions (not shown here). Cases S+C+F and U^G+C+F , on the other hand, change the orientation of the streaks to approximately $\pm 45^\circ$, resulting in a less realistic pattern when compared to the full ABL simulation. As mentioned before, this is a result of the incomplete force balance of these two cases, either driven by a shear or by a pressure term, which changes the alignment of the main flow. Thus, the inclusion of all terms as in case $S+U^G+C+F$ is essential for a more realistic representation of the ASL. Nevertheless, the shallow domain will not be able to capture the large and very large scale motions that fill the full ABL, and studies where these features are important must span the full depth of the ABL and the length of these structures.

87 4 Conclusion

While there is increasing research efforts examining the minimal requirements on domain size for wall-bounded flows over roughness elements (e.g., Mac-Donald et al. (2017)), recent studies (Su and Paw U 2023) have shown that simulating the entire ABL depth, as opposed to a limited region, is ideal to represent the full extent of the roughness and logarithmic layers above forests,

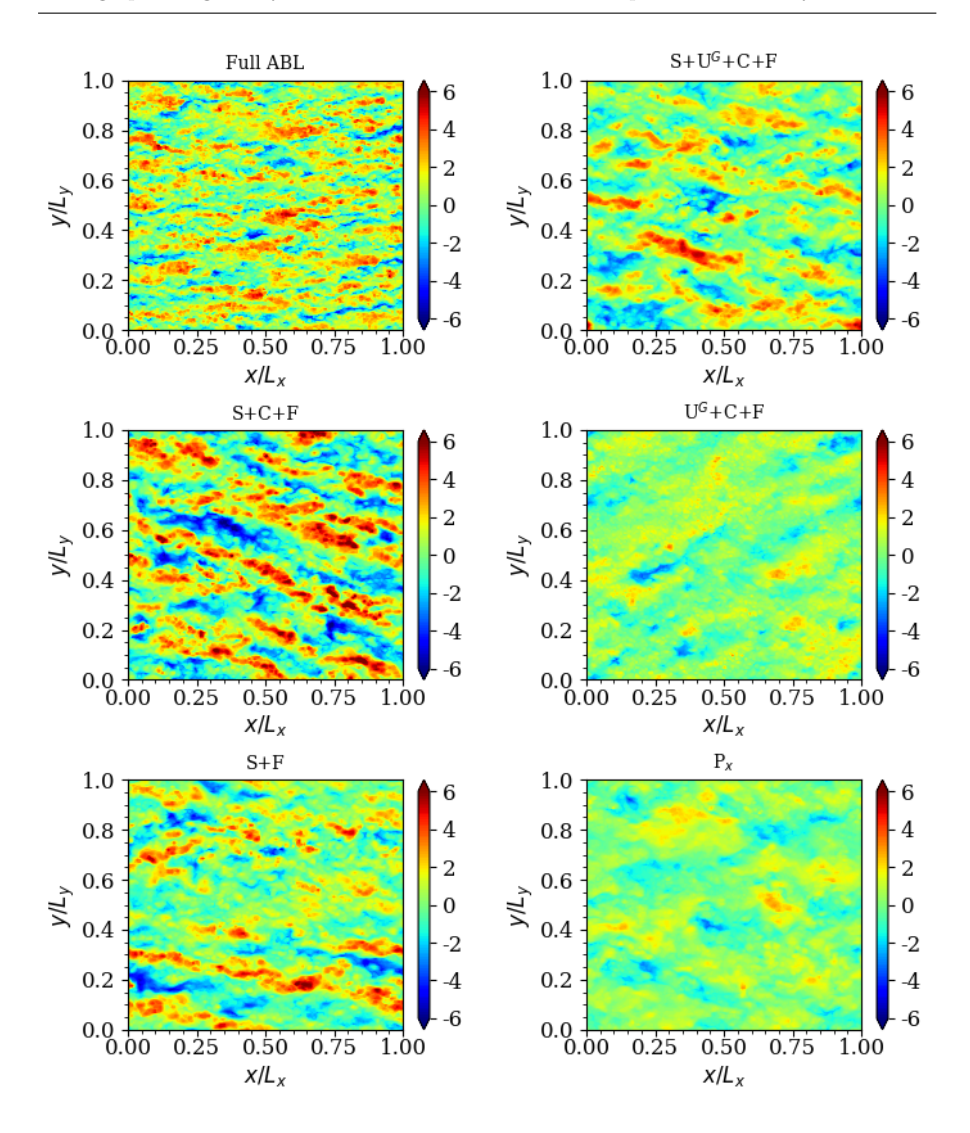


Fig. 3 Horizontal (x-y) slices of the instantaneous u'/u_* field across simulations sampled at $z \approx 100$ m. L_x and L_y represent the domain length in the streamwise and cross-stream directions, respectively.

as well as to more accurately capture shear stress budget terms. Nonetheless, the resolution required by such simulations is still prohibitive in most research applications, and would consume significantly more energy than a minimal domain. Although the recent development of Graphics Processing Unit (GPU)-based codes are promising options towards faster and more efficient simulations (Sauer and Muñoz-Esparza 2020), whether to expend any given computing resource in spanning the full ABL depth to capture the largest scales or focus

on better resolving the surface features and the turbulence therein remains a compromise that must be settled based on the application at hand. Alternative approaches that can be considered are the use of nested and/or stretched domains, where the ABL extent is represented by an independent coarse grid in the case of nesting, or progressively larger Δz in case of stretching, while the canopy (limited to a shallower domain) can be solved at a higher resolution (Patton et al. 2003; Cassiani et al. 2008; Huang et al. 2011). Nonetheless, these approaches have not been widely adopted due to the complexity of modifying existing codes and the intricate challenges associated with interfacing the two grids. Instead, most studies of canopies or with an ASL focus continue to use only one shallow domain due to it simplicity and suitability for conducting a large number of simulations. The present study is aimed at providing guidelines for setting up such single shallow domain simulations.

To that end, we investigated the impact of different driving forces and top boundary conditions on first, second, and third order moments, as well as coherent structures. Our results indicate that mean velocity profiles are relatively insensitive to the LES setup, although the wind angle varies from case to case. Increased disagreement was observed for higher order statistics. In particular, we show that the most commonly adopted configuration in simulations of canopy flows (streamwise pressure gradient, no Coriolis, zero stress and scalar flux at the top) might result in unrealistic profiles. For instance, not only do fluxes decrease much faster with height than predicted from full ABL simulation, but there is also an asymmetry in the velocity field distribution away from the canopy. Although similar results had been reported in the past (Watanabe 2004) over canopy flows, pressure driven flows are still the most common approach used to drive flows above complex terrains.

We propose a LES setup combining pressure and shear driven flows, as well as the inclusion of the Coriolis term. We show that this simulation replicates the expected flux profiles in the ASL, and agrees better with the full ABL simulation for variances (especially for u and v), and turbulent kinetic energy. We thus recommend it as a point of departure in future studies, with potential modifications and refinements to the setup we have here, depending on the goal of these future simulations. We also note that the values and angle of the stress and fluxes needed at the top boundary can be estimated from a single, relatively low resolution run of the full ABL. This approach is in some-sort a simplified offline nesting of the two simulations. Finally, for researchers with faster codes and more available computational resources, we also recommend a more detailed quantitative comparison of higher-order statistics profiles for the different setups at higher resolution, where the full ABL is simulated at the same grid spacing as the shallow domains.

Acknowledgements This work is supported by the Army Research Office under contract W911NF2010216, by the National Science Foundation under grant AGS2128345, and by the Cooperative Institute for Modeling the Earth System at Princeton University under Award NA18OAR4320123 from the National Oceanic and Atmospheric Administration. We would like to acknowledge high-performance computing support from Cheyenne (Computa-

- 445 tional and Laboratory 2019) provided by NCAR's Computational and Information Systems
- 446 Laboratory, sponsored by the National Science Foundation, under projects UPRI0007 and
- 447 UPRI0021.

448 Data Availability

- The data used to reproduce all figures can be found at https://www.dropbox.
- 450 com/scl/fo/8y50nixud2283yoi87zon/h?rlkey=sgjxxfs7o021h706i1mki9zt7&
- $_{451}$ dl=0. They Will be upload to Zenodo upon final acceptance of the
- paper.

453 Appendix A: Grid Convergence of the Full ABL Simulation

- Below we compare profiles of up to third-order statistics in the ABL obtained
- $_{455}$ $\,$ using a low resolution (LR) and a high-resolution (HR) domain. The respective
- number of grid points are $144 \times 144 \times 108$ (LR) and $288 \times 288 \times 216$ (HR),
- while the remaining characteristics of the simulation are identical.

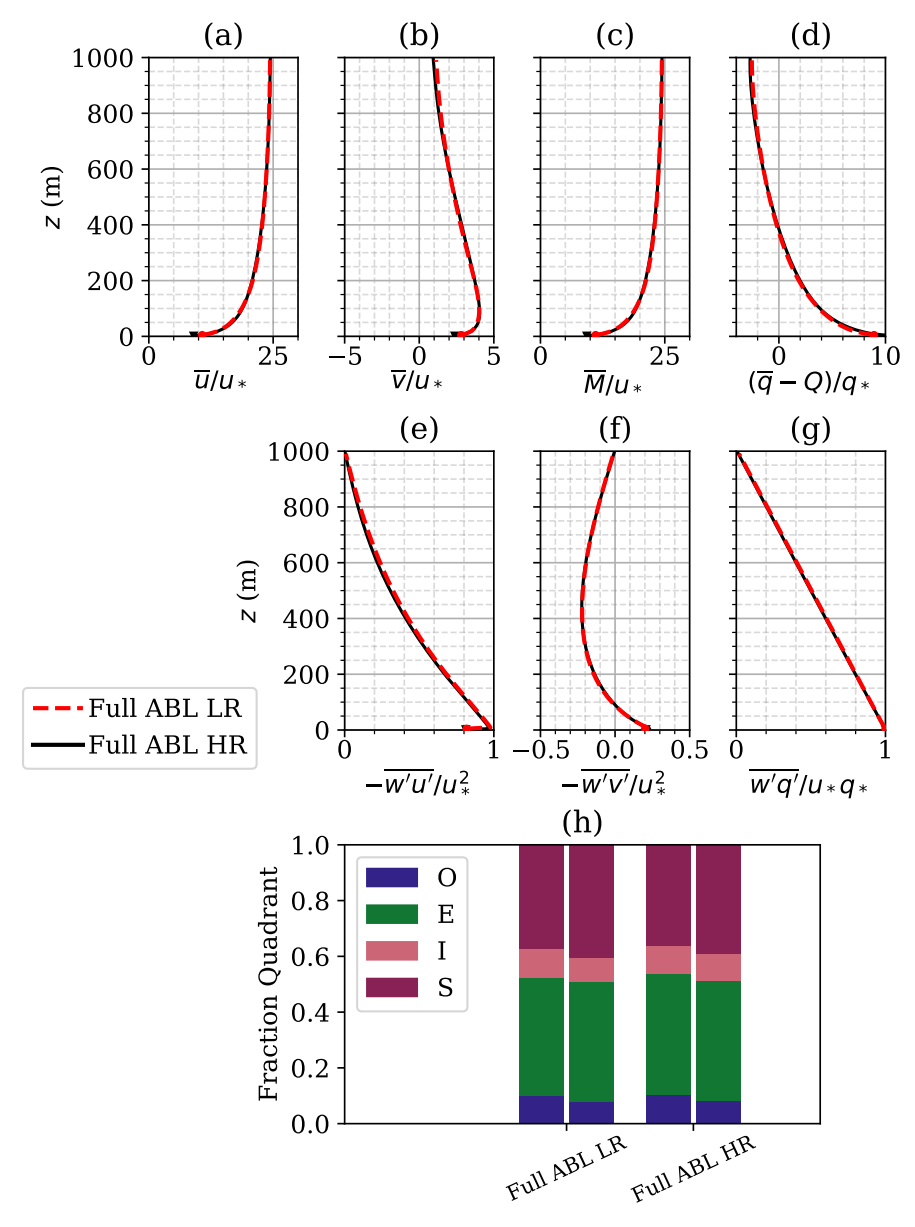


Fig. 4 Same as Figure 1, where now two cases are considered: results for the full ABL simulation using $144 \times 144 \times 108$ grid points (Full ABL LR) and $288 \times 288 \times 216$ grid points (Full ABL HR).

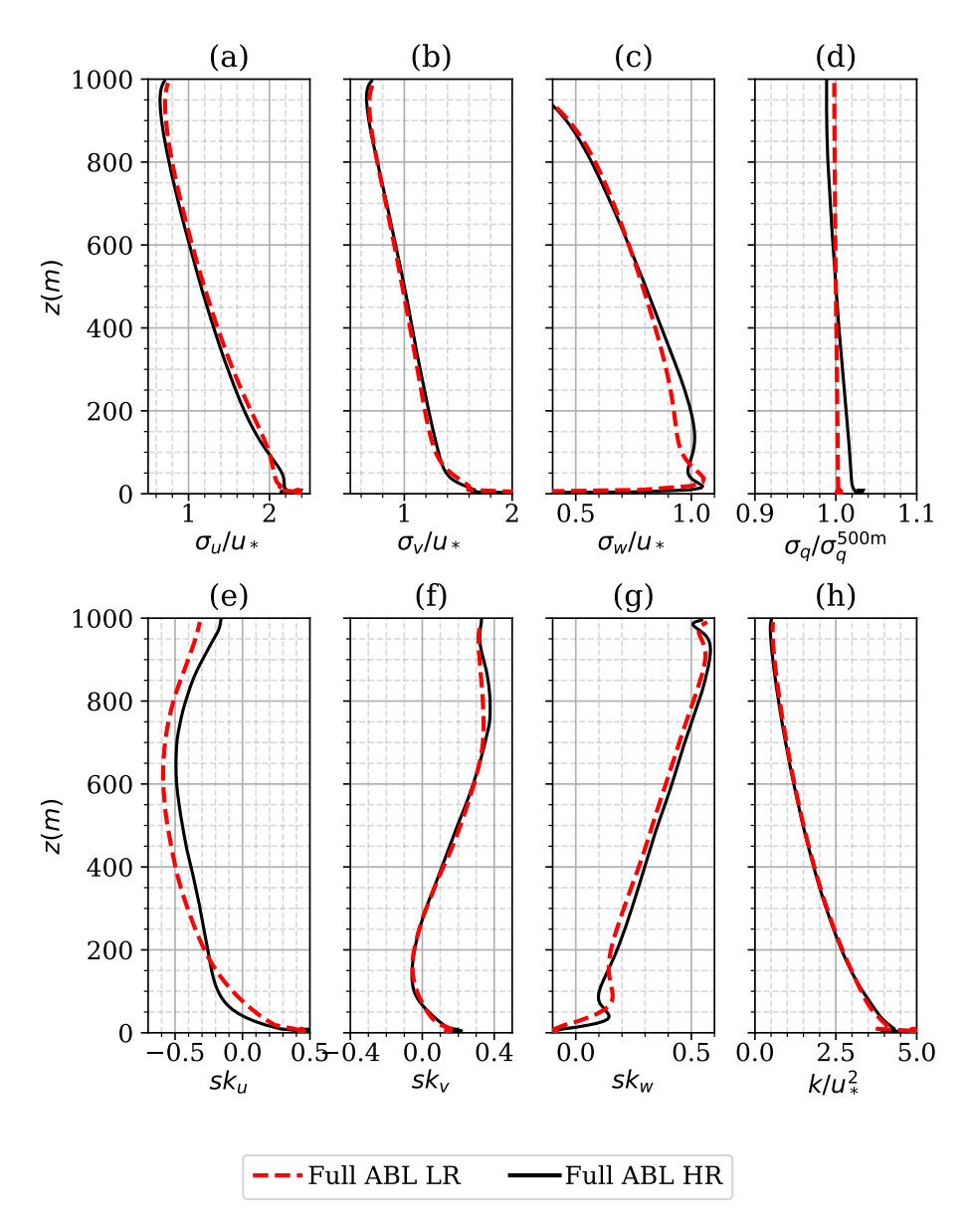


Fig. 5 Same as Figure 2, where now two cases are considered: results for the full ABL simulation using $144 \times 144 \times 108$ grid points (Full ABL LR) and $288 \times 288 \times 216$ grid points (Full ABL HR).

Appendix B

For reference, this section compares cases 2 and 6 from Table 1 with the inclusion of a canopy. The same details described in section 2 are used, where now an additional drag term D_i is added to the momentum equation (2) to represent a sink of momentum imposed by the trees,

$$D_i = -C_D a(z) \widetilde{u}_i |\widetilde{u}_i|. \tag{6}$$

 C_D is the drag coefficient (= 0.25 in the present paper) and a(z) is the leaf-area density profile, where the leaf-area index LAI = $\int_0^h a(z)dz = 2$ in the present study. A source term $S_c(z)$, representing scalar q emitted by the canopy, is additionally included in equation (3). The same leaf-area density and scalar source profiles from Su et al. (1998) were used in our simulations, and were represented by the lowest 10 grid points of the domain. With $N_z = 108$, we thus have $L_z/h = 10.8$ and $h \approx 13$ m.

To ensure a constant scalar flux in the case $S+U^G+C+F$, the subgrid scale flux component at the top includes both surface and canopy flux contributions, i.e.,

$$\pi_{\text{top}} = \pi_{\text{bottom}} + \sum_{c=0}^{z=h} S_c.$$
 (7)

Finally, the turbulent scales u_* and q_* are computed above the canopy. Comparison of both simulations is shown in Figures 6 and 7. As with the simulations over flat terrain in the body of the paper, significant differences can be noted with the S+ U^G +C+F case displaying more realistic vertical patterns.

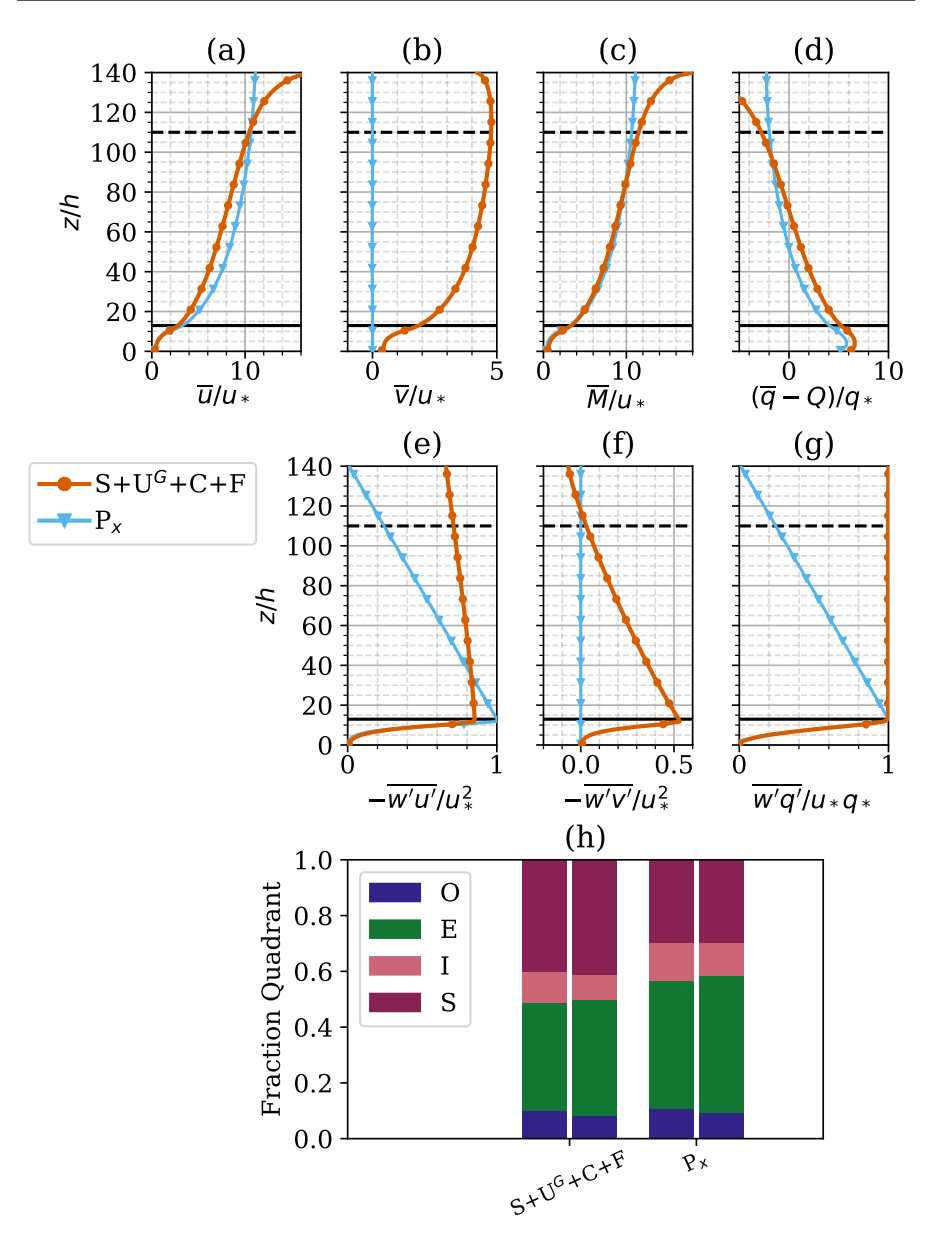


Fig. 6 Same as Figure 1, where two canopy flows are considered. Simulation $S+U^G+C+F$ contains top stress, pressure gradient (geostrophic forcing), Coriolis and constant flux at the top, while the second case is solely driven by a streamwise pressure term. The same resolution was used for both simulations ($144 \times 144 \times 108$ grid points). Continuous black line represents the canopy top, while dashed black line represents the height above which a sharp gradient is observed when a top stress drives the flow.

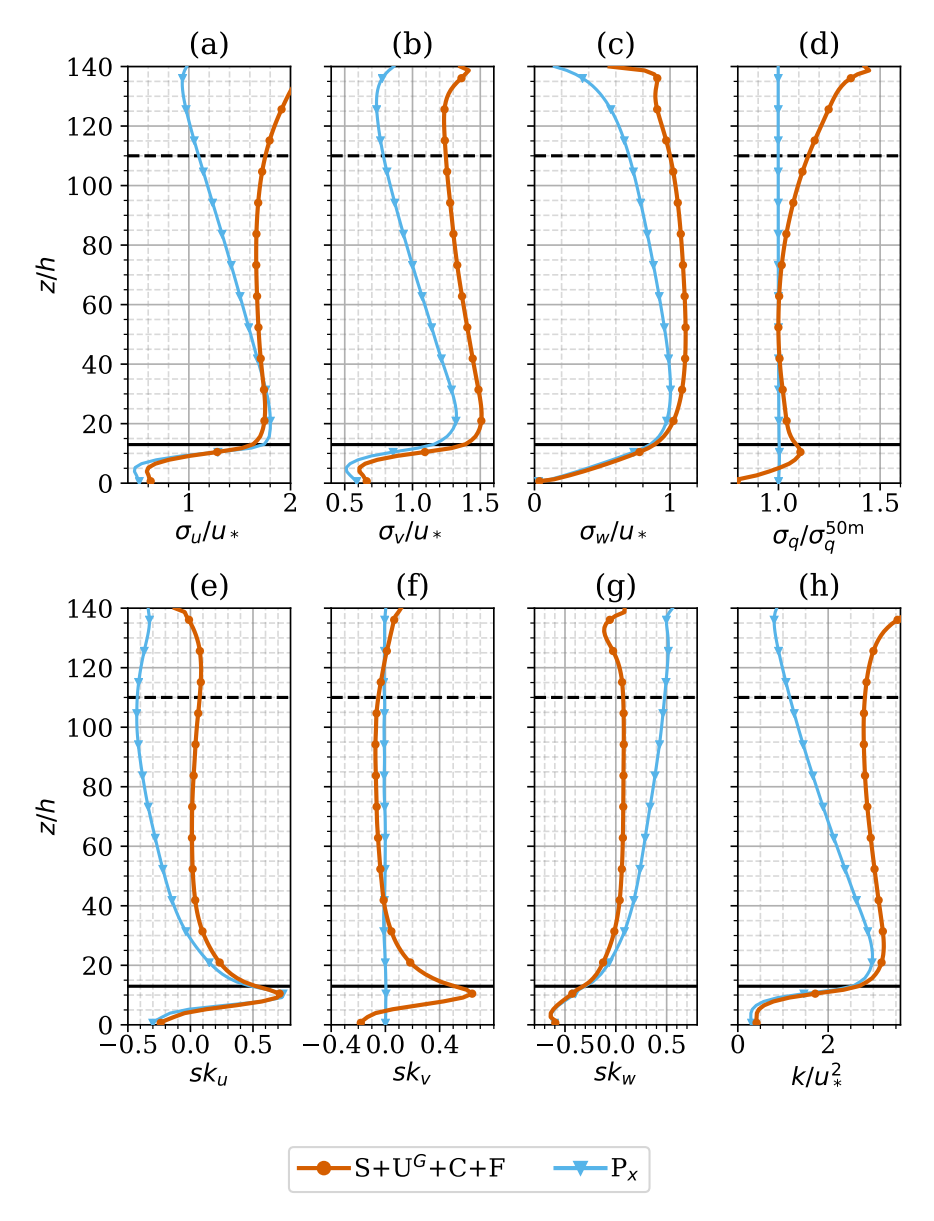


Fig. 7 Same as Figure 2, where two canopy flows are considered. Simulation $S+U^G+C+F$ contains top stress, pressure gradient (geostrophic forcing), Coriolis and constant flux at the top, while the second case is solely driven by a streamwise pressure term. The same resolution was used for both simulations ($144 \times 144 \times 108$ grid points). Continuous black line represents the canopy top, while dashed black line represents the height above which a sharp gradient is observed when a top stress drives the flow.

References

501

502

- Albertson JD, Katul GG, Wiberg P (2001a) Relative importance of local and regional controls on coupled water, carbon, and energy fluxes. Advances in Water Resources 24(9):1103–1118, DOI https://doi.org/10.1016/
 S0309-1708(01)00042-2
- Albertson JD, Kustas WP, Scanlon TM (2001b) Large-eddy simulation over heterogeneous terrain with remotely sensed land surface conditions.

 Water Resources Research 37(7):1939–1953, DOI https://doi.org/10.1029/2000WR900339
- Allouche M, Bou-Zeid E, Iipponen J (2023) The influence of synoptic wind
 on land—sea breezes. Quarterly Journal of the Royal Meteorological Society
 DOI 10.1002/qj.4552
- Anderson W, Li Q, Bou-Zeid E (2015) Numerical simulation of flow over urbanlike topographies and evaluation of turbulence temporal attributes. Journal of Turbulence 16(9):809–831, DOI 10.1080/14685248.2015.1031241
- Avissar R, Schmidt T (1998) An evaluation of the scale at which groundsurface heat flux patchiness affects the convective boundary layer using large-eddy simulations. Journal of the Atmospheric Sciences 55(16):2666– 2689, DOI 10.1175/1520-0469(1998)055\(2666:AEOTSA\)\(2.0.CO;\)2
- Bailey BN, Stoll R (2013) Turbulence in sparse, organized vegetative canopies:
 A large-eddy simulation study. Boundary-Layer Meteorology 147, DOI 10.
 1007/s10546-012-9796-4
- Bastankhah M, Porté-Agel F (2014) A new analytical model for wind-turbine wakes. Renewable Energy 70:116 123, DOI 10.1016/j.renene.2014.01.002
 - Berg J, Patton EG, Sullivan PP (2020) Large-eddy simulation of conditionally neutral boundary layers: A mesh resolution sensitivity study. Journal of the Atmospheric Sciences 77(6):1969 1991, DOI https://doi.org/10.1175/JAS-D-19-0252.1
- Bertoldi G, Albertson JD, Kustas WP, Li F, Anderson MC (2007) On the opposing roles of air temperature and wind speed variability in flux estimation from remotely sensed land surface states. Water Res Research 43(10):W10,433, DOI 10.1029/2007WR005911
- Bou-Zeid E, Meneveau C, Parlange M (2005) A scale-dependent lagrangian
 dynamic model for large eddy simulation of complex turbulent flows. Physics
 of Fluids 17(2):025,105, DOI 10.1063/1.1839152
- Calaf M, Meneveau C, Meyers J (2010) Large eddy simulation study of fully
 developed wind-turbine array boundary layers. Physics of Fluids 22(1):1 –
 16, DOI 10.1063/1.862466
- Cassiani M, Katul GG, Albertson JD (2008) The effects of canopy leaf area index on airflow across forest edges: Large-eddy simulation and analytical results. Boundary-Layer Meteorology 126, DOI https://doi.org/10.1007/s10546-007-9242-1
- Chatelain P, Backaert S, Winckelmans G, Kern S (2013) Large eddy simulation
 of wind turbine wakes. Flow, Turbulence and Combustion 91(3):587 605,
 DOI 10.1007/s10494-013-9474-8

533

537

539 540

541

543

544

545

547

548

551

552

553

554

555

558

559

560

- Churchfield MJ, Lee S, Michalakes J, Moriarty PJ (2012) A numerical study of
 the effects of atmospheric and wake turbulence on wind turbine dynamics.
 Journal of Turbulence 13:N14, DOI 10.1080/14685248.2012.668191
- Computational, Laboratory IS (2019) Cheyenne: HPE/SGI ICE XA system
 (university community computing). boulder, CO: National center for atmospheric research. DOI 10.5065/D6RX99HX
- Deardorff JW (1970) Preliminary results from numerical integrations of the unstable planetary boundary layer. Journal of Atmospheric Sciences 27(8):1209
 1211, DOI https://doi.org/10.1175/1520-0469(1970)027(1209:PRFNIO)2.
 0.CO;2
 - Esau IN (2007) Amplification of turbulent exchange over wide Arctic leads: Large-eddy simulation study. J Geophys Res 112(D8):D08,109
- Fogarty J, Bou-Zeid E (2023) The atmospheric boundary layer above the marginal ice zone: Scaling, surface fluxes, and secondary circulations.

 Boundary-Layer Meteorology DOI 10.1007/s10546-023-00825-x
 - Ghannam K, Bou-Zeid E (2021) Baroclinicity and directional shear explain departures from the logarithmic wind profile. Quarterly Journal of the Royal Meteorological Society 147(734):443–464, DOI https://doi.org/10.1002/qj. 3927
 - Grylls T, van Reeuwijk M (2021) Tree model with drag, transpiration, shading and deposition: Identification of cooling regimes and large-eddy simulation. Agricultural and Forest Meteorology 298-299:108,288, DOI https://doi.org/10.1016/j.agrformet.2020.108288
 - van Heerwaarden CC, Mellado JP, De Lozar A (2014) Scaling Laws for the Heterogeneously Heated Free Convective Boundary Layer. J Atmos Sci 71(11):3975–4000, DOI 10.1175/jas-d-13-0383.1
 - Hellsten A, Luukkonen SM, Steinfeld G, Kanani-Sühring F, Markkanen T, Järvi L, Lento J, Vesala T, Raasch S (2015) Footprint evaluation for flux and concentration measurements for an urban-like canopy with coupled lagrangian stochastic and large-eddy simulation models. Boundary-Layer Meteorology 157, DOI 10.1007/s10546-015-0062-4
 - Hellsten A, Ketelsen K, Sühring M, Auvinen M, Maronga B, Knigge C, Barmpas F, Tsegas G, Moussiopoulos N, Raasch S (2021) A nested multi-scale system implemented in the large-eddy simulation model palm model system 6.0. Geoscientific Model Development 14(6):3185–3214, DOI 10.5194/gmd-14-3185-2021
 - Heus T, van Heerwaarden CC, Jonker HJJ, Pier Siebesma A, Axelsen S, van den Dries K, Geoffroy O, Moene AF, Pino D, de Roode SR, Vilà-Guerau de Arellano J (2010a) Formulation of the dutch atmospheric large-eddy simulation (dales) and overview of its applications. Geoscientific Model Development 3(2):415–444, DOI 10.5194/gmd-3-415-2010
- Heus T, van Heerwaarden CC, Jonker HJJ, Pier Siebesma A, Axelsen S,
 van den Dries K, Geoffroy O, Moene AF, Pino D, de Roode SR, Vilà Guerau de Arellano J (2010b) Formulation of the dutch atmospheric large eddy simulation (dales) and overview of its applications. Geoscientific Model
 Development 3(2):415-444, DOI 10.5194/gmd-3-415-2010

571

573

574

575

576

577

578

579

581

582

583

585

586

589

590

591

592

593

594

597

598

600

- Hezaveh SH, Bou-Zeid E (2018) Mean kinetic energy replenishment mechanisms in vertical-axis wind turbine farms. Physical Review Fluids 3:94,606
- Huang J, Bou-Zeid E (2013) Turbulence and vertical fluxes in the stable atmospheric boundary layer. part i: A large-eddy simulation study. Journal of the Atmospheric Sciences 70:1513–1527, DOI 10.1175/JAS-D-12-0167.1
- Huang J, Cassiani M, Albertson JD (2009) The effects of vegetation density on coherent turbulent structures within the canopy sublayer: A large-eddy simulation study. Boundary-Layer Meteorology 133, DOI https://doi.org/10.1007/s10546-009-9423-1
- Huang J, Lee X, Patton EG (2011) Entrainment and budgets of heat, water vapor, and carbon dioxide in a convective boundary layer driven by time-varying forcing. Journal of Geophysical Research: Atmospheres 116(D6), DOI https://doi.org/10.1029/2010JD014938
- Huang J, Katul G, Albertson J (2013) The role of coherent turbulent structures in explaining scalar dissimilarity within the canopy sublayer. Environmental Fluid Mechanics 13, DOI 10.1007/s10652-013-9280-9
- Joshi P, Anderson W (2022) Surface layer response to heterogeneous tree canopy distributions: roughness regime regulates secondary flow polarity. Journal of Fluid Mechanics 946:A28, DOI 10.1017/jfm.2022.583
- Khanna S, Brasseur JG (1997) Analysis of monin-obukhov similarity from large-eddy simulation. Journal of Fluid Mechanics 345:251–286, DOI 10. 1017/S0022112097006277
- Klosterhalfen A, Moene A, Schmidt M, Scanlon T, Vereecken H, Graf A (2019) Sensitivity analysis of a source partitioning method for H₂O and CO₂ fluxes based on high frequency eddy covariance data: Findings from field data and large eddy simulations. Agricultural and Forest Meteorology 265:152 170, DOI https://doi.org/10.1016/j.agrformet.2018.11.003
- Kosović B, Curry JA (2000) A large eddy simulation study of a quasi-steady, stably stratified atmospheric boundary layer. Journal of the Atmospheric Sciences 57(8):1052 1068, DOI https://doi.org/10.1175/1520-0469(2000) 057(1052:ALESSO)2.0.CO;2
- Kumar V, Kleissl J, Meneveau C, Parlange MB (2006) Large-eddy simulation of a diurnal cycle of the atmospheric boundary layer: Atmospheric stability and scaling issues. Water Resources Research 42(6), DOI https://doi.org/10.1029/2005WR004651
- Li Q, Bou-Zeid E (2019) Contrasts between momentum and scalar transport over very rough surfaces. Journal of Fluid Mechanics 880:32–58, DOI 10. 1017/jfm.2019.687
- Li Q, Wang ZH (2018) Large-eddy simulation of the impact of urban trees on
 momentum and heat fluxes. Agricultural and Forest Meteorology 255:44–56,
 DOI https://doi.org/10.1016/j.agrformet.2017.07.011
- Li Q, Bou-Zeid E, Anderson W (2016a) The impact and treatment of the gibbs phenomenon in immersed boundary method simulations of momentum and scalar transport. Journal of Computational Physics 310:237–251, DOI 10.1016/j.jcp.2016.01.013

- Li Q, Bou-Zeid E, Anderson W, Grimmond S, Hultmark M (2016b) Quality and reliability of les of convective scalar transfer at high reynolds numbers. International Journal of Heat and Mass Transfer 102:959–970, DOI 10.1016/j.ijheatmasstransfer.2016.06.093
- Llaguno-Munitxa M, Bou-Zeid E (2018) Shaping buildings to promote street ventilation: A large-eddy simulation study. Urban Climate 26:76–94, DOI https://doi.org/10.1016/j.uclim.2018.08.006
 - Llaguno-Munitxa M, Bou-Zeid E, Hultmark M (2017) The influence of building geometry on street canyon air flow: Validation of large eddy simulations against wind tunnel experiments. Journal of Wind Engineering and Industrial Aerodynamics 165:115–130, DOI 10.1016/j.jweia.2017.03.007
- MacDonald M, Chung D, Hutchins N, Chan L, Ooi A, García-Mayoral R (2017) The minimal-span channel for rough-wall turbulent flows. Journal of Fluid Mechanics 816:5–42, DOI 10.1017/jfm.2017.69
 - Mao S, Leclerc MY, Michaelides EE (2008) Passive scalar flux footprint analysis over horizontally inhomogeneous plant canopy using large-eddy simulation. Atmospheric Environment 42(21):5446–5458, DOI https://doi.org/10.1016/j.atmosenv.2008.02.029
 - Maronga B, Gryschka M, Heinze R, Hoffmann F, Kanani-Sühring F, Keck M, Ketelsen K, Letzel MO, Sühring M, Raasch S (2015) The parallelized large-eddy simulation model (palm) version 4.0 for atmospheric and oceanic flows: model formulation, recent developments, and future perspectives. Geoscientific Model Development 8(8):2515–2551, DOI 10.5194/gmd-8-2515-2015
 - Maronga B, Banzhaf S, Burmeister C, Esch T, Forkel R, Fröhlich D, Fuka V, Gehrke KF, Geletič J, Giersch S, Gronemeier T, Groß G, Heldens W, Hellsten A, Hoffmann F, Inagaki A, Kadasch E, Kanani-Sühring F, Ketelsen K, Khan BA, Knigge C, Knoop H, Krč P, Kurppa M, Maamari H, Matzarakis A, Mauder M, Pallasch M, Pavlik D, Pfafferott J, Resler J, Rissmann S, Russo E, Salim M, Schrempf M, Schwenkel J, Seckmeyer G, Schubert S, Sühring M, von Tils R, Vollmer L, Ward S, Witha B, Wurps H, Zeidler J, Raasch S (2020) Overview of the palm model system 6.0. Geoscientific Model Development 13(3):1335–1372, DOI 10.5194/gmd-13-1335-2020
 - Mason PJ (1989) Large-eddy simulation of the convective atmospheric boundary layer. Journal of Atmospheric Sciences 46(11):1492 1516, DOI https://doi.org/10.1175/1520-0469(1989)046(1492:LESOTC)2.0.CO;2
 - Mirocha J, Kirkil G, Bou-Zeid E, Chow FK, Kosović B (2013) Transition and equilibration of neutral atmospheric boundary layer flow in one-way nested large-eddy simulations using the weather research and forecasting model. Monthly Weather Review 141(3):918 940, DOI https://doi.org/10.1175/MWR-D-11-00263.1
- Muñoz-Esparza D, Shin HH, Sauer JA, Steiner M, Hawbecker P, Boehnert J,
 Pinto JO, Kosović B, Sharman RD (2021) Efficient graphics processing unit
 modeling of street-scale weather effects in support of aerial operations in
 the urban environment. AGU Advances 2(2):e2021AV000,432, DOI https:
 //doi.org/10.1029/2021AV000432

- Pan Y, Chamecki M, Isard SA (2014) Large-eddy simulation of turbulence and particle dispersion inside the canopy roughness sublayer. Journal of Fluid Mechanics 753:499–534, DOI 10.1017/jfm.2014.379
- Patton EG, Davis KJ, Barth MC, Sullivan PP (2001) Decaying scalars emitted by a forest canopy: A numerical study. Boundary-Layer Meteorology 100, DOI 10.1023/A:1019223515444
- Patton EG, Sullivan PP, Davis KJ (2003) The influence of a forest canopy on top-down and bottom-up diffusion in the planetary boundary layer. Quarterly Journal of the Royal Meteorological Society 129(590):1415–1434, DOI https://doi.org/10.1256/qj.01.175
- Potomac-Hudson Environmental Team (2010) National center for atmospheric research wyoming supercomputer center: Environmental assessment and finding of no significant impact
- Raupach MR, Finnigan JJ, Brunei Y (1996) Coherent eddies and turbulence in vegetation canopies: The mixing-layer analogy. Boundary-Layer Meteorology 78, DOI 10.1007/BF00120941
- Sanemitsu T, Ikegaya N, Okaze T, Finnigan JJ (2023) Appropriate momentum provision for numerical simulations of horizontally homogeneous urban canopies using periodic boundary conditions. Boundary-Layer Meteorology pp 1573–1472, DOI 10.1007/s10546-023-00823-z
 - Sauer JA, Muñoz-Esparza D (2020) The fasteddy® resident-gpu accelerated large-eddy simulation framework: Model formulation, dynamical-core validation and performance benchmarks. Journal of Advances in Modeling Earth Systems 12(11):e2020MS002,100, DOI https://doi.org/10.1029/2020MS002100

680

681

- Shaw RH, Patton EG (2003) Canopy element influences on resolved- and subgrid-scale energy within a large-eddy simulation. Agricultural and Forest Meteorology 115(1):5–17, DOI https://doi.org/10.1016/S0168-1923(02) 00165-X
- Shaw RH, Schumann U (1992) Large-eddy simulation of turbulent flow above and within a forest. Boundary-Layer Meteorology 61, DOI 10.1007/ BF02033994
- Shin HH, Muñoz-Esparza D, Sauer JA, Steiner M (2021) Large-eddy simulations of stability-varying atmospheric boundary layer flow over isolated buildings. Journal of the Atmospheric Sciences 78(5):1487 1501, DOI https://doi.org/10.1175/JAS-D-20-0160.1
- Stoll R, Gibbs JA, Salesky ST, Anderson W, Calaf M (2020) Large-eddy simulation of the atmospheric boundary layer. Boundary-Layer Meteorology 177,
 DOI 10.1007/s10546-020-00556-3
- Su HB, Paw U KT (2023) Large-eddy simulation of reynolds stress budgets in
 and above forests in neutral atmospheric boundary layers. Boundary-Layer
 Meteorology DOI 10.1007/s10546-022-00758-x
- Su HB, Shaw RH, Paw KT, Moeng CH, Sullivan PP (1998) Turbulent statistics
 of neutrally stratified flow within and above a sparse forest from large-eddy
 simulation and field observations. Boundary-Layer Meteorology 88, DOI
 10.1023/A:1001108411184

- Sullivan PP, Patton EG (2011) The effect of mesh resolution on convective
 boundary layer statistics and structures generated by large-eddy simulation.
 Journal of the Atmospheric Sciences 68(10):2395 2415, DOI https://doi.
 org/10.1175/JAS-D-10-05010.1
- Sullivan PP, McWilliams JC, Moeng CH (1996) A grid nesting method for
 large-eddy simulation of planetary boundary-layer flows. Boundary-Layer
 Meteorology 80, DOI https://doi.org/10.1007/BF00119016
- Talbot C, Bou-Zeid E, Smith J (2012) Nested mesoscale large-eddy simulations with wrf: Performance in real test cases. Journal of Hydrometeorology 13:1421–1441, DOI 10.1175/JHM-D-11-048.1
 - Troldborg N, Sørensen JN, Mikkelsen R, Sørensen NN (2014) A simple atmospheric boundary layer model applied to large eddy simulations of wind turbine wakes. Wind Energy 17(4):657 669, DOI 10.1002/we.1608
- Watanabe T (2004) Large-eddy simulation of coherent turbulence structures associated with scalar ramps over plant canopies. Boundary-Layer Meteorology 112, DOI 10.1023/B:BOUN.0000027912.84492.54
- Wu YT, Porté-Agel F (2011) Large-eddy simulation of wind-turbine wakes:
 Evaluation of turbine parametrisations. Boundary-Layer Meteorology
 138(3):345 366, DOI 10.1007/s10546-010-9569-x
- Xie ZT, Castro IP (2009) Large-eddy simulation for flow and dispersion in
 urban streets. Atmospheric Environment 43(13):2174–2185, DOI https://doi.org/10.1016/j.atmosenv.2009.01.016
- Yue W, Parlange MB, Meneveau C, Zhu W, van Hout R, Katz J (2007)
 Large-eddy simulation of plant canopy flows using plant-scale representation. Boundary-Layer Meteorology 124, DOI 10.1007/s10546-007-9173-x